Available online at www.sciencedirect.com

SciVerse ScienceDirect

Ceramics International 38 (2012) 5461–5468

CERAMICS INTERNATIONAL

www.elsevier.com/locate/ceramint

Enhanced ionic conductivity of Sm, Gd-doped ceria induced by modification of powder synthesis procedure

N. Cioateră [a,*], V. Pârvulescu [b], A. Rolle [c], R.N. Vannier [c]

[a] *University of Craiova, Department of Chemistry, Calea Bucuresti 107I, Craiova, Romania*
[b] *Romanian Academy, Institute of Physical Chemistry, Splaiul Independentei 202, Bucharest, Romania*
[c] *Unité de Catalyse et de Chimie du Solide, Equipe de Chimie du Solide, UMR CNRS 8181, ENSCL/UST Lille 1, BP 90 108, 59652 Villeneuve d'Ascq Cedex, France*

Received 10 February 2012; received in revised form 21 March 2012; accepted 23 March 2012
Available online 1 April 2012

Abstract

Nanostructured $Ce_{0.85}Gd_{0.05}Sm_{0.10}O_{2-\delta}$ powders have been obtained by a classical and a modified Pechini method. The textural parameters of the synthesized powders were evaluated using N_2 adsorption–desorption. X-ray diffraction (XRD) showed that the powders were single phase with fluorite-type structure. The dilatometry measurements evidenced a strong influence of the synthesis procedure of Gd, Sm-co-doped ceria on its sintering behavior. A decrease in powder sintering temperature down to 1200 °C was obtained when Triton X-100 was added into the synthesis reaction mixture. The AC impedance spectroscopy of the sintered pellets was also performed in the 200–800 °C temperature range, in air. The sample prepared using the non-ionic surfactant exhibited higher ionic conductivities and lower activation energies than the sample synthesized by classical Pechini method over the entire investigated temperature range.

Keywords: A. Sintering; B. Defects; C. Electrical conductivity; Doped ceria

1. Introduction

Development of solid oxide fuel cells (SOFCs) is currently focused toward lowering their operating temperature to about 700 °C. This will require new materials and new processing technologies to ensure adequate electrode kinetics and internal resistance of the cell.

Ceria-based materials have been considered as one of the most promising ionic conductors for intermediate-temperature SOFC (IT-SOFC) and sensor applications, due to their higher oxygen ionic conductivity than yttria-stabilized zirconia (YSZ) [1]. Even if pure ceria is a poor ionic conductor, it was proved that its ionic conductivity significantly increases by doping with aliovalent cations, such as Gd^{3+}, Sm^{3+}, Pr^{3+}, etc. [2–4]. The best results in terms of ionic conductivity were obtained for Gd and Sm single doped ceria. Thus, Gd-doped ceria was extensively investigated as an electrolyte material for IT-SOFC. A further improvement in ceria ionic conductivity was obtained by multiple doping. Yamamura et al. [5] also reported a decrease of activation energy of conduction after co-doping due to the suppression of oxygen vacancy ordering. In a recent study, Wang et al. [6] concluded that Gd, Sm-co-doped samples having the composition $Ce_{0.85}Gd_{0.15-y}Sm_yO_{1.925}$ ($0.05 \leq y \leq 0.1$) exhibit higher ionic conductivities than corresponding single doped samples. Besides material composition, the properties–microstructure–processing relationships have to be investigated in order to optimize the SOFC materials [7].

One major inconvenient of ceria-based SOFC electrolytes is their high sintering temperatures (usually exceeding 1400 °C) to get dense samples. At these elevated temperatures, the grain growth rates are high, resulting in large grains and poor mechanical stability. Recent studies revealed that by using adequate sintering additives and synthesis procedures, the temperature required to densify the ceria-based electrolytes can be reduced [8,9]. Moreover, it is well documented that the microstructure of polycrystalline materials has a strong influence on their electrical conductivity as it induces variations in grain and grain boundary properties [10]. Unlike solid state synthesis method, the wet chemical synthesis procedures allow a better control of powder microstructure by simply tuning the

---

* Corresponding author. Tel.: +40 251597048; fax: +40 251597048.
E-mail address: nicoletacioatera@yahoo.com (N. Cioateră).

0272-8842/$36.00 © 2012 Elsevier Ltd and Techna Group S.r.l. All rights reserved.
http://dx.doi.org/10.1016/j.ceramint.2012.03.058

synthesis parameters. Among them, the sol–gel method allows the preparation of powders with nanometric particle size [11]. Cost-effective, nontoxic and biodegradable structure-directing agents, such as Triton X-100, have been widely involved in the preparation of ordered mesoporous oxides, especially silicas [12]. The goal of our research was to use Triton X-100 in order to prepare nanostructured co-doped ceria with improved properties based on the surfactant self-assembly process.

In this study, a modified sol–gel method developed by Pechini was used for the synthesis of $Ce_{0.85}Gd_{0.05}Sm_{0.10}O_{2-\delta}$ powders. The Pechini method has been modified by adding Triton X-100 (a non-ionic templating agent) into the reaction mixture with the aim to evidence the influence of the templating agent on the structure, texture, morphology, thermal behavior, and electrical conductivity of Gd, Sm-doped ceria samples.

2. Experimental

2.1. Powder synthesis

Powders with composition $Ce_{0.85}Gd_{0.05}Sm_{0.10}O_{2-\delta}$ have been synthesized from hydrated nitrate precursors via two methods. One procedure involved in the mixed oxide synthesis is the Pechini method, in which the citric acid is used for metal cation chelation. In this procedure, a 0.4 M aqueous solution of nitrate precursors was prepared with respect to the compound stoichiometry. Citric acid (CA) was subsequently added in a proportion which corresponds to the molar ratio CA:Me = 4.5. The as-obtained solution was heated at 80 °C under vigorous stirring and under reflux for the complete dissolution of the metallic precursors. Ethylene-glycol (EG) was further added in a molar ratio CA:EG = 2 in order to initiate the polyesterification reactions, resulting in the formation of a homogenous sol. After removal of the solvent excess under vacuum, using a rotary evaporator, the resulting gel was dried in air at 120 °C. This led to a brownish solid resin (CGS sample) which was further calcined at 550 °C in air for 6 h. A modified Pechini method was also used for the synthesis of Gd, Sm-co-doped ceria powder. In this procedure, a non-ionic surfactant (Triton X-100, 8 vol.%) was initially added to the aqueous precursor solution which was further processed as previously mentioned (CGSTr sample).

2.2. Powder physico-chemical characterizations

Thermal analysis (TG) of the solid resins was performed using a Perkin Elmer thermogravimetric analyzer. The samples were heated from room temperature to 800 °C in synthetic air with a heating rate of 10 °C/min.

BET surface areas of the powders were measured by nitrogen adsorption. N_2 adsorption–desorption was carried out at 77 K with a TriStar 3000 analyzer (Micromeritics). The samples were degassed at 150 °C for 12 h prior each measurement.

To identify the phases in the calcined powders, X-ray diffraction (XRD) was carried out. A D8 Bruker diffractometer equipped with Vantec1 linear detector was used for the analysis of powder in the range of $2\theta = 20–75°$ with a 0.0148° step size. A LaB_6 standard was used to derive the diffractometer resolution. The lattice parameters were refined using the Fullprof software. Each peak profile was fitted using the option “Fit” of the WinPlotr software [13]. Crystallite sizes were calculated using the Halder–Wagner–Langford (HWL) relationship [14].

A Jeol 5300 scanning electron microscope (SEM) was used to characterize the microstructure of the powder.

To establish the adequate sintering treatment of the synthesized powders, linear thermal behavior of all samples were measured using a horizontal differential dilatometer (Linseis L75). Measurements were performed in air from room temperature to 1350 °C with a heating rate of 5 °C/min. The green pellets were prepared by uniaxially pressing of the calcined powders in a 5 mm stainless steel die. The resulting pellet had an about 4 mm width.

2.3. Pellet processing and characterization

The calcined powders were uniaxially pressed in a 10 mm diameter stainless steel die and further isostatically pressed under 180 MPa to obtain green pellets. These pellets were further sintered at 1200 °C for 5 h using a heating rate of 3 °C/min.

The relative densities of the sintered pellets were calculated as the ratio between the real density (evaluated from pellet weight and its geometrical dimensions) and theoretical one (calculated taking into account the lattice parameter).

A D8 Advance Bruker diffractometer equipped with a SolX dispersive detector was used for the analysis of the sintered pellets. The diffractograms were recorded in the 20–70° range with a 0.02° step and a 1.5 s/step counting time using the Cu Kα radiation. The lattice parameters and crystallite sizes were determined using the same procedure as in the case of powders.

A Jeol 5300 scanning electron microscope (SEM) was used to characterize the microstructure of the ceramic.

The sintered pellets were subsequently prepared for electrochemical measurements. The pellets were polished with SiC papers with various grids to obtain planar surface. Gold was used as electrodes. Therefore, a gold thin film was deposited onto their opposite faces via sputtering (at 15 mA for 4 min); subsequently, gold paste was brushed onto both sides of the pellets. The as-obtained pellets were then fired at 600 °C for 1 h to remove the organic components. The AC impedance spectroscopy measurements were performed in air, in the temperature range 300–800 °C, using a SI 1266 Solartron Impedance/Gain-Phase Analyzer in the 30 MHz–0.10 Hz frequency range. The amplitude of the AC perturbation signal was 10 mV and the measurements were carried out at open circuit potential. The ionic conductivities of the samples were obtained after fitting with a commercial software package (ZView) provided by Scribner.

3. Results and discussion

3.1. Powder physico-chemical characterization and morphology

As shown in Fig. 1, thermogravimetric analysis indicates that the decompositions of the resins obtained after gel drying take place in several steps, as follows. In a first step, the removal of residual water occurs between 25 and 120 °C. The subsequent step can be attributed to the reaction between nitrate and citrate group, while the final step corresponds to the pyrolysis of the residual organic constituents. It can be seen that all organics have been removed at temperatures above 400 °C. A higher total mass loss was evidenced for the resin obtained using Triton X-100 as structure-directing agent. This behavior can be due to its greater organic content as compared to the sample prepared without templating agent. Consequently, the solid resins obtained in this study by classic and modified Pechini methods were further thermally processed by calcination at 550 °C in air for 6 h.

The textural properties of the synthesized powders were determined by nitrogen adsorption–desorption analysis. The adsorption–desorption isotherms and the corresponding Barrett–Joyner–Halenda (BJH) pore size distributions for the powders prepared using different synthesis procedures are shown in Fig. 2. The sample obtained by classical Pechini route exhibits a type II isotherm, with a H3 hysteresis loop, which can be assigned to the nitrogen condensation in open slit-type capillaries. When Triton X-100 was added into the reaction mixture, changes in isotherm shape and hysteresis loop type were evidenced. Thus, CGSTr sample exhibited a combination of type I and II isotherms, with a H4 type hysteresis loop. This type of hysteresis loop associated with the type I isotherm indicates a microporous structure with a narrow pore size distribution. The investigated samples exhibited both framework-confined and textural porosity. The presence of framework-confined porosity is indicated by the occurrence of an adsorption step in the 0.1–0.5 relative pressure range, while the appearance of a hysteresis loop in the 0.5–1.0 relative pressure range can be ascribed to the textural porosity [15].

The calculated Brunauer–Emmett–Teller (BET) surface area, the mean pore radius, and the total pore volume of both samples are shown in Table 1. An increase of the specific surface area and a decrease of pore radius, as well as the narrowing of the pore size distribution can be noticed after the addition of non-ionic surfactant in the reaction mixture.

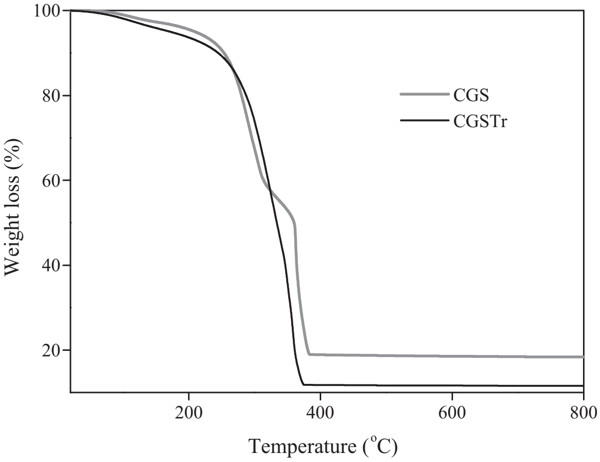

Fig. 1. DTG curves of the solid resins synthesized using the classic (CGS) and modified (CGSTr) Pechini methods.

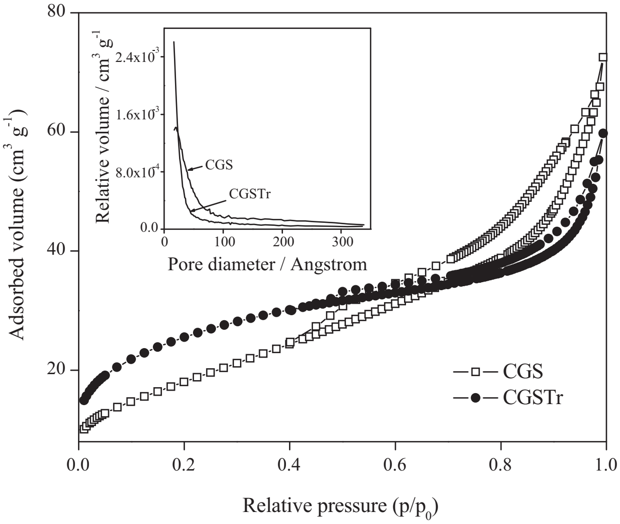

Fig. 2. N_2 adsorption–desorption isotherms of the powders (BJH pore size distribution is shown in the insert).

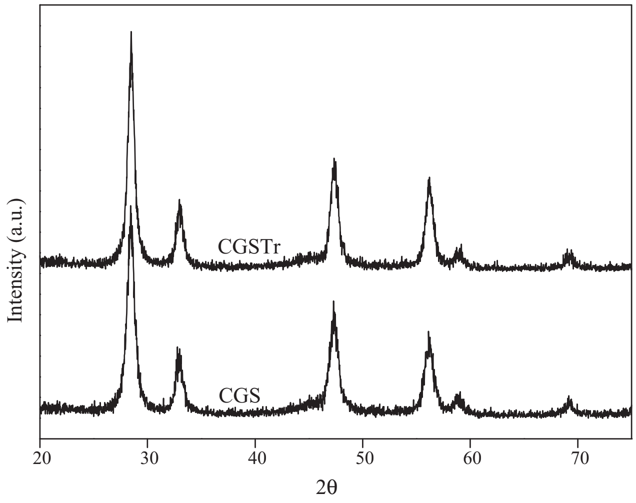

Fig. 3. XRD patterns of the powders.

Crystalline phase analysis of the synthesized powders was carried out using XRD (Fig. 3). The XRD patterns of CGS and CGSTr samples are characteristic of the fluorite-type structure and seem to indicate that single phase ceramics have been obtained. The nanocrystalline nature of the powders was also evidenced by XRD (Fig. 3). The crystallite size values shown in Table 1 have been obtained by the analysis of Bragg peak widths. While for CGSTr sample the crystallite sizes obtained from XRD data are in good agreement with particle sizes calculated using BET surface areas, indicating that these particles are mostly single crystals, in the case of CGS sample a sintering of primary crystallites occurs. The unit cell parameters of fluorite phase are shown in Table 1. As was expected from effective ionic radii considerations, an increase of the lattice parameter after Gd, Sm–co-doping of ceria is evidenced (5.4107(6) Å for CeO_2). The Gd^{3+} and Sm^{3+} radii in VIII-fold coordination are 1.053 and 1.079 Å, respectively, which are higher than the one characteristic to the host Ce^{4+}

Table 1
Textural and structural parameters of synthesized powders.

Sample	Lattice parameter[a], Å	D_{XRD} [b], nm	Pore radius, nm	Pore volume, $\mathrm{cm^3\,g^{-1}}$	S_{BET} [c], $\mathrm{m^2\,g^{-1}}$	D_{BET} [d], nm
CGS	5.42(3)	7.5	3.3	0.112	66	12.62
CGSTr	5.42(7)	9.5	2.0	0.092	91	9.11

[a] Lattice parameters of fluorite phase.
[b] Crystallite dimensions of fluorite phase calculated from XRD data.
[c] BET specific surface area.
[d] Particle dimensions calculated using BET specific surface.

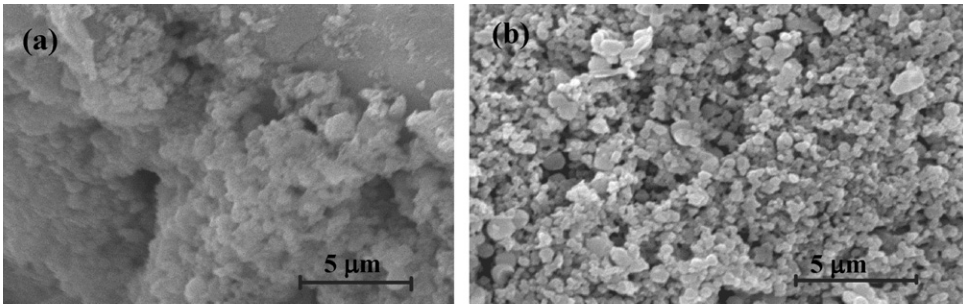

Fig. 4. SEM images of (a) CGS and (b) CGSTr calcined powders.

(0.97 Å). The addition of Triton X-100 in the reaction mixture results seems to have no influence on the lattice parameter value and consequently, on dopant solubility into ceria host matrix.

Fig. 4 shows the SEM micrographs of the calcined powders. The particles prepared by both methods proved to be irregular in shapes and present a strong tendency toward aggregation. Nevertheless, the agglomerates in the CGS sample were denser than the ones from CGSTr powder obtained using Triton X-100 as structure-directing agent, in agreement with the physico-chemical parameters shown in Table 1.

3.2. Powder sintering behavior

The sintering behavior of the synthesized powders was evaluated using the uniaxial dilatometry technique, the measurements being performed from r.t. up to 1350 °C. The linear shrinkage of both investigated samples is shown in Fig. 5(a). As can be seen, CGS sample did not attain the full shrinkage in the investigated temperature range. For CGSTr sample, ∼27% shrinkage occurred up to about 1200 °C, a further increase in temperature leading to the thermal expansion of the sample. Fig. 5(b) shows the variation of shrinkage rate with temperature. It can be noticed that the sintering process of co-doped ceria samples is strongly influenced by the synthesis procedure. Thus, the CGS sample exhibits two shrinkage maxima: the first one at about 660 °C and the second at ∼1120 °C, the last having a higher shrinkage rate than the first. The sintering of CGSTr sample is a multi-step process, with shrinkage maxima at about 750, 900 and 1100 °C. The shrinking rates corresponding to these maxima increase with increasing temperature. The two shrinkage maxima from lower temperatures can be ascribed to the breakdown of CGSTr bimodal porous structure, while the wider maximum from higher temperatures may arise from particle sintering. The shrinkage stopped at about 1200 °C and the subsequent thermal

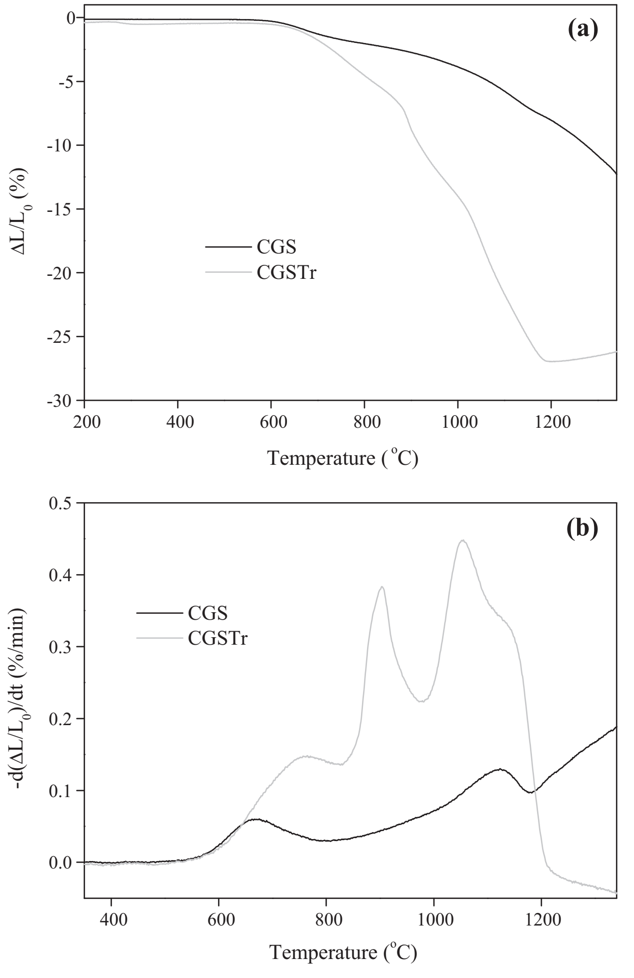

Fig. 5. The dependence of linear shrinkage rate with the temperature for the samples synthesized by the two different methods.

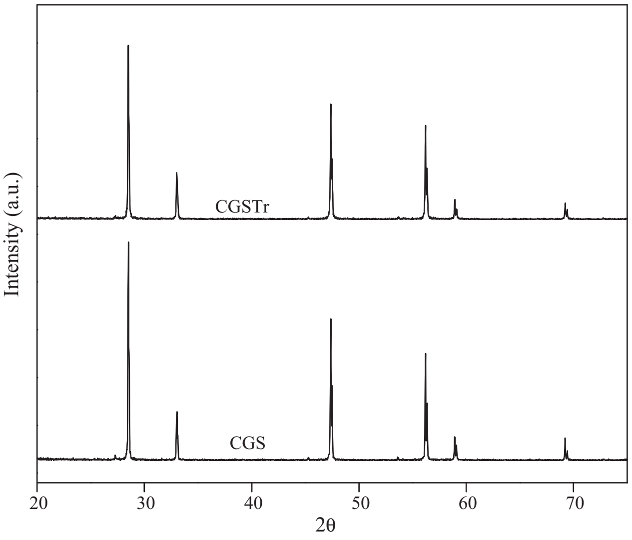

Fig. 6. XRD patterns of sintered pellets.

expansion of the material at temperatures higher than 1200 °C indicates the completion of sintering process. In the case of the sample prepared by classical Pechini route (CGS), even if the sintering starts at about 600 °C (similar to the CGSTr sample), the first shrinkage maximum shifts toward lower temperature, while the following two maxima are shifted toward higher temperatures (the maximum attributed to particles sintering exceeds the apparatus limits). The higher sintering temperature of CGS sample compared to the one of CGSTr can be assigned to its higher agglomeration degree. Based on these results, the optimal sintering temperature of CGSTr sample was found to be 1200 °C.

3.3. Pellet characterization

All synthesized powders have been shaped into circular pellets, followed by sintering at 1200 °C for 5 h. In Fig. 6, the XRD patterns of sintered pellets are shown. Both pellets exhibited only the characteristic peaks of fluorite-type phase. The lattice parameters and the crystallite dimensions in sintered pellets are presented in Table 2.

It can be noticed that both samples exhibit higher lattice parameter values than the corresponding powders. The presence of Triton X-100 in the reaction mixture seems to have only a slight influence on the crystallite dimensions and grain sizes, as XRD data analysis (Table 2) and SEM images (Fig. 7) revealed.

An increase with at least one order of magnitude of crystallite dimensions after sintering for both samples was evidenced. The surface micrographs of sintered pellets obtained from powders prepared by both methods revealed grains with heterogeneous sizes and shapes (Fig. 7).

3.4. Electrochemical characterization

Electrochemical characterization of the sintered pellets (obtained from the powders synthesized using Pechini and modified Pechini methods) was performed by electrochemical impedance spectroscopy (EIS). EIS analysis allows the separation of the bulk and grain-boundary contributions to the overall sample resistance. Impedance spectra of the samples are given in Fig. 8. The real and imaginary parts of impedance represented on the axes were normalized considering the ratio between electrode area and electrolyte thickness. The contributions of grain bulk, grain boundary, and electrode/electrolyte interface can be evidenced as three successive arcs at high, intermediate, and low frequencies, respectively. Only the contributions of grain bulk and grain boundary will be considered in the following discussion. As the temperature increases, the shift toward higher frequencies of bulk and grain boundary arcs was evidenced for both investigated samples. Moreover, the resistivity of the sample shifts toward smaller values when a structure-directing agent is used in the powder synthesis procedure.

Table 2
Structural parameters and activation energies for oxide ion conduction in the investigated samples.

Sample	Lattice parameter, Å	D_{XRD}, nm	$E_{\mathrm{a,bulk}}$, eV		σ_0 ($\times 10^{-6}\ \Omega^{-1}\ \mathrm{cm}^{-1}$ K)	$E_{a,gb}$, eV	$E_{a,gb} - E_{a,bulk}$, eV
			<450 °C	>450 °C			
CGS	5.432(5)	38.4	0.86	0.62	2.78	1.48	0.60
CGSTr	5.430(8)	43.7	0.89	0.59	7.65	1.36	0.44

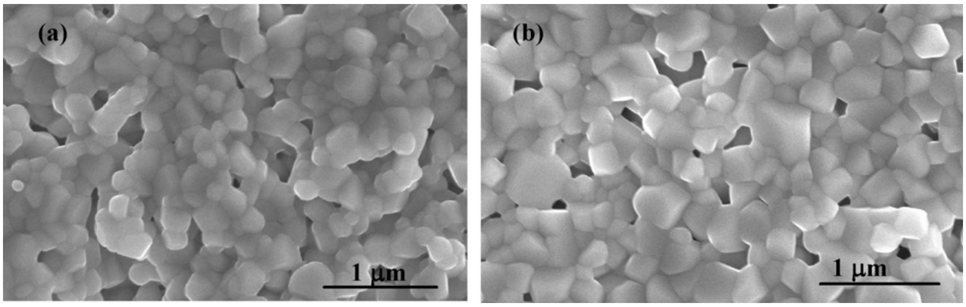

Fig. 7. SEM micrographs of sintered pellets: (a) CGS and (b) CGSTr.

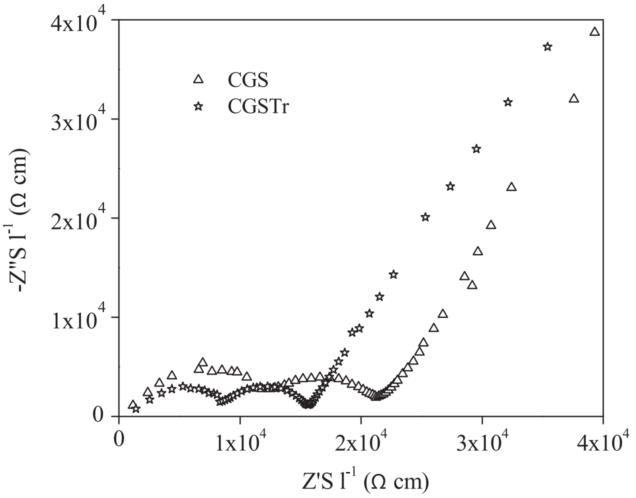

Fig. 8. AC impedance spectra of the sintered pellets at 300 °C.

By fitting the impedance spectra with the (R-CPE)$_1$(R-CPE)$_2$(R-CPE)$_3$ equivalent circuit, the bulk and grain boundary resistances were obtained. Considering the sample geometries, the resistances were converted into the corresponding electrical conductivities. The resistivities of bulk and grain boundary have similar values, this behavior being characteristic to moderately blocking grain boundaries [16]. When temperature exceeds 400 °C, the arc corresponding to bulk contribution disappears due to the increase of relaxation frequencies (the decrease of time constants) over the equipment limit. In order to distinguish between the contributions of grain and grain boundary to the total conductivity at temperatures above 400 °C, a linear behavior of grain boundary conductivity in Arrhenius plot was considered [17].

The Arrhenius plots of total conductivities are shown in Fig. 9a. CGSTr sample exhibited the highest values of total ionic conductivity over the entire investigated temperature range (200–800 °C). This behavior is determined by the increase in both bulk and grain boundary conductivity after the addition of Triton X-100 in powder synthesis procedure (Fig. 9b and c).

Fig. 9b shows the Arrhenius plots of bulk conductivities for the investigated samples. It can be seen that the CGSTr sample exhibits higher bulk conductivity values than CGS one over the entire investigated temperature range. As previous studies revealed, in the high oxygen partial pressure range, doped ceria exhibits ionic conduction by oxygen vacancy diffusion [18]. The values of activation energy for bulk conduction (Table 2) corresponding to the investigated samples indicate that ionic conduction mechanism prevails.

The Arrhenius plots of bulk conductivities (Fig. 9b) exhibit a curvature in the temperature range 400–500 °C, usually ascribed to the transition from associated to dissociated defects. In the low temperature range, the coulombic attractions between defects with opposite charges leads to the formation of defect associates $(Gd'_{Ce}V_O^{\bullet\bullet})^{\bullet}$, $(Sm'_{Ce}V_O^{\bullet\bullet})$, $(Gd'_{Ce}V_O^{\bullet\bullet}Gd'_{Ce})^x$, $(Sm'_{Ce}V_O^{\bullet\bullet}Sm'_{Ce})^x$, $(Sm'_{Ce}V_O^{\bullet\bullet}Gd'_{Ce})^x$, etc.). Therefore, the activation energy for bulk conductivity is the sum of migration and association enthalpies. At temperatures higher than 500 °C this parameter identifies only with migration enthalpy. The activation energy values for both samples are shown in Table 2. It can be noticed that CGSTr sample posses lower migration

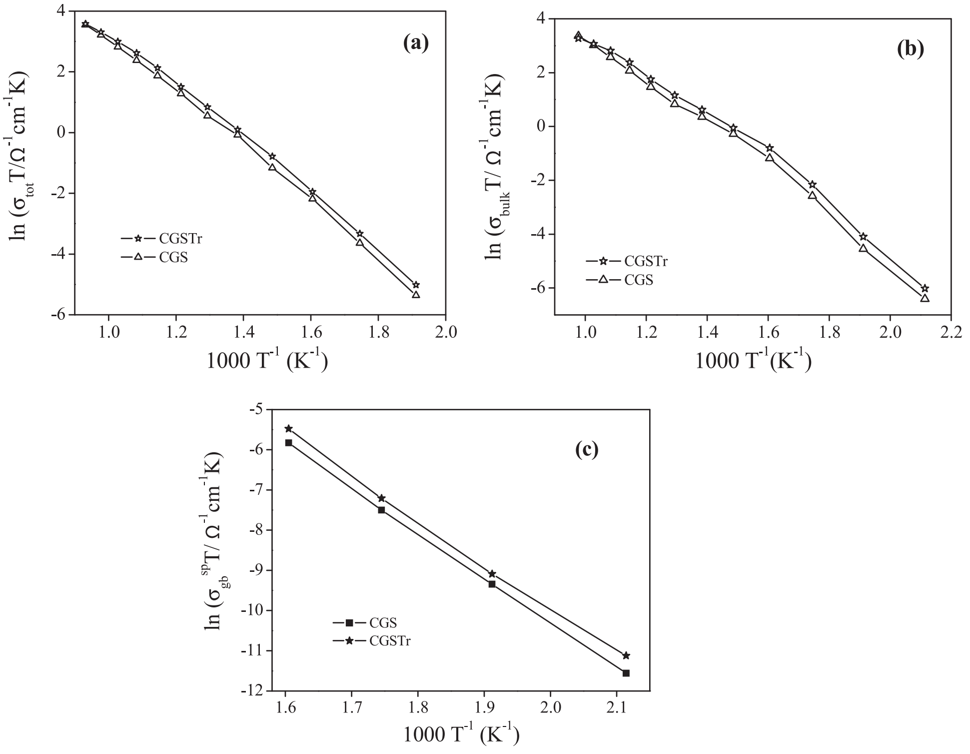

Fig. 9. Arrhenius plots of: (a) total ionic conductivity; (b) bulk conductivity; and (c) specific grain-boundary conductivity of investigated samples.

enthalpy and higher association enthalpy than CGS one, while the sum of them slightly changes. The dependence of ionic conductivity on different parameters is given by the following equation [19]:

$$\sigma = \frac{A}{WkT} \exp\left(\frac{\Delta S_m + \Delta S_a}{k}\right) \exp\left(-\frac{\Delta H_m + \Delta H_a}{kT}\right) \tag{1}$$

where ΔS_m and ΔH_m are the migration entropy and enthalpy, respectively, and ΔS_a and ΔH_a are the association entropy and enthalpy; W is the number of associate orientations. According to this equation, the higher ionic conductivity of CGSTr sample can be attributed to the increase in configurational entropy as pre-exponential term ($\sigma_0 = A/(Wk) \exp[(\Delta S_m + \Delta S_a)/k]$) increase when Triton X-100 is used in the synthesis procedure (Table 2).

The lower value of pre-exponential term for CGS sample can be ascribed to the partial ordering of defects. Previous studies evidenced the formation of nanodomains (large-scale defect associations) with well-developed structures. Thus, Mori and co-workers [20] shown that for Gd-doped ceria with Gd contents higher than 10 at.% nano-sized domains with C-type structure are formed for samples sintered at 1400 °C. Moreover, by lowering the sintering temperature a shift of lower nanodomain formation limit toward higher dopant concentrations was observed. In a recent study, Wang et al. [21] shown that at a dopant concentration lower than 20 at.% Gd, small dispersed clusters with pyrochlore-type structure will be formed in ceria host matrix, the driving force of clustering being cation diffusion.

As the lattice parameter of both CGS and CGSTr samples increases after sintering at 1200 °C with no additional peaks of secondary phases in XRD patterns, it was assumed that defect clusters with pyrochlore-type structure are formed. Moreover, as CGS sample exhibits a higher lattice parameter than CGSTr one, it may posses a greater defect cluster density. The formation of defect clusters leads to a decrease of ionic conductivity as they act as traps for oxygen vacancies. Therefore, in the low temperature range, CGSTr sample exhibits higher ionic conductivity than CGS sample, while at temperatures greater than 700 °C the samples have similar conductivity values.

Thus, the differences in the bulk conductivities of the samples can be mainly ascribed to the different distribution of the dopant cations in the ceria host lattice, based on the variation of the powder synthesis conditions, as both samples possess relative densities higher than 90%. The addition of Triton X-100 into the reaction mixture seems to restrain the formation of defect clusters during sintering, leading to an increase in ionic conductivity.

It is well-known that sample microstructure and geometry have a great influence on its grain-boundary conductivity. In order to compare the grain-boundary conduction behavior, the specific grain-boundary conductivity (σ_{gb}) of the two investigated samples was calculated using the relaxation frequency (f_{gb}) [7]:

$$\sigma_{gb} = 2\pi f_{gb} \varepsilon_0 \varepsilon_r \tag{2}$$

with $f_{gb} = (2\pi R_{gb} C_{gb})^{-1}$, where ε_0 is the vacuum permittivity, ε_r is the dielectric constant (for ceria-based materials $\varepsilon_r \approx 30$), R_{gb} and C_{gb} being the grain-boundary resistance and capacitance, respectively. The resulted values of specific grain-boundary are shown in Fig. 9c. The differences between the two investigated samples can be ascribed to space charge effects. The presence of an excess of oxygen vacancies in the grain-boundary core is the main driving force for acceptor (Gd'_{Ce} and Sm'_{Ce}) segregation at the grain boundaries during the sintering stage, being also responsible for the oxygen vacancy depletion in the grain-boundary space-charge layers. The dopant concentration profile at grain boundaries remains constant during EIS measurements, while the oxygen vacancy concentration in the grain boundaries changes with temperature as they are mobile charge carriers in the investigated temperature range (the Mott–Schottky case). Based on defect cluster densities of the samples, we may assume that the dopant concentration at grain boundaries in CGS sample is lower than the one corresponding to the CGSTr one. Consequently, the concentration of oxygen vacancies residing in the space charge layers is higher for CGSTr than for CGS sample, thus explaining the variation of specific grain-boundary conductivity with sample preparation.

According to the Mott–Schottky case of the space charge model for grain boundary (which assumes a constant concentration of acceptor dopant across the space charge layer), the Schottky barrier height ($\Delta\varphi$) can be obtained by solving the following equation [22]:

$$\frac{\sigma_{bulk}}{\sigma_{gb}} = \frac{\exp((2e\,\Delta\varphi)/kT)}{(4e\,\Delta\varphi)/kT} \tag{3}$$

where e is the elementary charge, k is the Boltzmann constant, and T is the absolute temperature. The values of potential difference between space charge core and bulk ($\Delta\varphi$) are plotted in Fig. 10 as a function of temperature.

The positive potential difference is attributed to the higher oxygen vacancy concentration of grain-boundary core than the bulk. The $\sigma_{bulk}/\sigma_{gb}$ ratio, as well as space-charge potential decrease with increasing temperature for both investigated

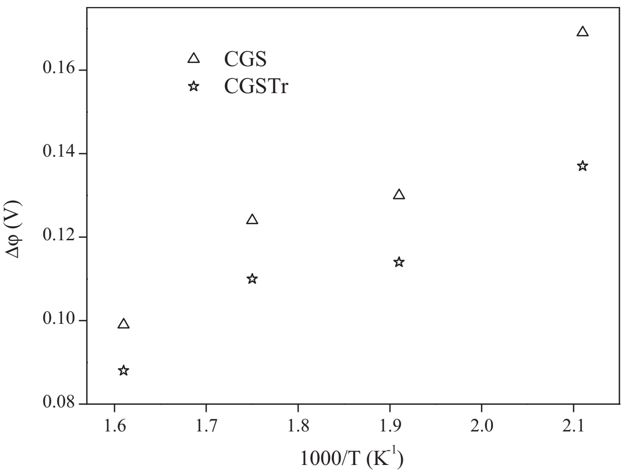

Fig. 10. Evolution of space-charge potential with temperature for co-doped ceria samples.

samples. When the space-charge potential attains such a low value for which $\sigma_{bulk}/\sigma_{gb}$ approach unity, the blocking effect of grain boundaries disappears. Moreover, when Triton X-100 is used in the synthesis procedure of co-doped ceria powder, a decrease in space-charge potential was obtained. The difference between the activation energies for grain boundary and bulk conductivities is a function of the space-charge potential and of its dependence on temperature [23]:

$$E_{a,gb} - E_{a,bulk} = (2e\,\Delta\varphi - kT)\left[1 + \frac{1}{T\,\Delta\varphi}\frac{d\,\Delta\varphi}{d(1/T)}\right] \qquad (4)$$

The average values of activation energy differences calculated using Eq. (4) are in good agreement with the experimental values (Table 2). Therefore, the variation in activation energy of grain-boundary conductivity with the synthesis procedure can be ascribed to changes in their space-charge potential, as the bulk activation energy is independent of $\Delta\varphi$.

4. Conclusions

$Ce_{0.85}Gd_{0.05}Sm_{0.10}O_{2-\delta}$ nanostructured materials with fluorite-type structure have been obtained using a classical and a modified Pechini method. The addition of non-ionic templating agent into the reaction mixture influences the oxide powder texture and morphology, thus leading to differences in powder sintering behavior. Therefore, a decrease of powder sintering temperature can thus be achieved. Impedance spectroscopy measurements revealed that the synthesis procedure of ceria-based mixed oxides has a strong influence on their electrical conduction behavior. The evaluation of bulk, grain boundary, and total conductivities of the investigated samples evidenced an increase in the electrical conductivities of ceria co-doped samples when non-ionic templating agent is used, probably due to the differences regarding dopant distribution into the grain bulk and grain boundaries. Using Triton X-100 into the synthesis procedure an increase in bulk ionic conductivity was attained by restraining the defect cluster formation during sintering. This also leads to an increase of oxygen vacancy concentration in the space-charge layers; consequently, the grain-boundary conductivity increase.

Acknowledgement

This work was partially supported by the strategic grant POSTDRU/89/1.5/S/61968, Project ID 61968 (2009), co-financed by the European Social Fund within the Sectorial Operational Program Human Resources Development 2007–2013.

References

[1] V.V. Kharton, F.M. Figueiredo, L. Navarro, E.N. Naumovich, A.V. Kovalevsky, A.A. Yaremchenko, et al., Ceria-based materials for solid oxide fuel cells, Journal of Materials Science 36 (2001) 1105–1117.

[2] Z. Tianshu, P. Hing, H. Huang, J. Kilner, Ionic conductivity in the CeO_2–Gd_2O_3 system ($0.05 \leq Gd/Ce \leq 0.4$) prepared by oxalate coprecipitation, Solid State Ionics 148 (2002) 567–573.

[3] P. Shuk, M. Greenblatt, Hydrothermal synthesis and properties of mixed conductors based on $Ce_{1-x}Pr_xO_{2-\delta}$ solid solutions, Solid State Ionics 116 (1999) 217–223.

[4] H. Inaba, H. Tagawa, Ceria-based solid electrolytes, Solid State Ionics 83 (1996) 1–16.

[5] H. Yamamura, E. Katoh, M. Ichikawa, K. Kakinuma, T. Mori, H. Haneda, Multiple doping effect on the electrical conductivity in the $(Ce_{1-x-y}La_xM_y)O_{2-\delta}$ (M = Ca, Sr) system, Electrochemistry 68 (2000) 455–459.

[6] F.Y. Wang, B.Z. Wan, S. Cheng, Study on Gd^{3+} and Sm^{3+} co-doped ceria based electrolytes, Journal of Solid State Electrochemistry 9 (2005) 168–173.

[7] D. Pérez-Coll, D. Marrero-López, P. Núñez, S. Piñol, J.R. Frade, Grain boundary conductivity of $Ce_{0.8}Ln_{0.2}O_{2-\delta}$ (Ln = Y, La, Gd, Sm) with and without Co-doping, Electrochimica Acta 51 (2006) 6463–6469.

[8] S.K. Tadokoro, T.C. Porfirio, R. Muccillo, E.N.S. Muccillo, Synthesis, sintering and impedance spectroscopy of 8 mol% yttria-doped ceria solid electrolyte, Journal of Power Sources 130 (2004) 15–21.

[9] H. Yoshida, T. Inagaki, Effects of additives on the sintering properties of samaria-doped ceria, Journal of Alloys and Compounds 408–412 (2006) 632–636.

[10] B.L. Cushing, V.L. Kolesnichenko, C.J. O'Connor, Recent advances in the liquid-phase syntheses of inorganic nanoparticles, Chemical Reviews 104 (2004) 3893–3946.

[11] S. Boskovic, D. Djurovic, Z. Dohcevic-Mitrovic, Z. Popovic, M. Zinkevich, F. Aldinger, Self-propagating room temperature synthesis of nanopowders for solid oxide fuel cells (SOFC), Journal of Power Sources 145 (2005) 237–242.

[12] D. Zhao, Q. Huo, J. Feng, B.F. Chmelka, G.D. Stucky, Nonionic triblock and star diblock copolymer and oligomeric surfactant syntheses of highly ordered, hydrothermally stable, mesoporous silica structures, Journal of the American Ceramic Society 120 (1998) 6024–6036.

[13] T. Roisnel, J. Rodriguez-Carvajal, WinPLOTR: a Windows tool for powder diffraction patterns analysis, in: R. Delhez, E.J. Mittenmeijer (Eds.), Proceedings of the Seventh European Powder Diffraction Conference (EPDIC 7), 2000, pp. 118–123, see also http://www-llb.cea.fr/Fullweb/winplotr/winplotr.htm.

[14] J.I. Langford, D. Louër, E.J. Sonneveld, J.W. Visser, Applications of total pattern fitting to a study of crystallite size and strain in zinc oxide powder, Powder Diffraction 1 (1986) 211–221.

[15] P.T. Tanev, T.J. Pinnavaia, Mesoporous silica molecular sieves prepared by ionic and neutral surfactant templating: a comparison of physical properties, Chemistry of Materials 8 (1996) 2068–2079.

[16] J. Fleig, The grain boundary impedance of random microstructures: numerical simulations and implications for the analysis of experimental data, Solid State Ionics 150 (2002) 181–193.

[17] D. Pérez-Coll, P. Núñez, J.C. Ruiz-Morales, J. Peña-Martinez, J.R. Frade, Re-examination of bulk and grain boundary conductivities of $Ce_{1-x}Gd_xO_{2-\delta}$ ceramics, Electrochimica Acta 52 (2007) 2001–2008.

[18] S. Omar, E.D. Wachsman, J.C. Nino, A co-doping approach towards enhanced ionic conductivity in fluorite-based electrolytes, Solid State Ionics 177 (2006) 3199–3203.

[19] L. Li, L. Lu, H. Xie, Electrolytic domain boundary between ionic and electronic conduction of doped ceria, Journal of Materials Science & Technology 14 (1998) 451–456.

[20] F. Ye, T. Mori, D.R. Ou, J. Zou, G. Auchterlonie, J. Drennan, Compositional and structural characteristics of nano-sized domains in gadolinium-doped ceria, Solid State Ionics 179 (2008) 827–831.

[21] B. Wang, R.J. Lewis, A.N. Cormack, Computer simulations of large-scale defect clustering and nanodomain structure in gadolinia-doped ceria, Acta Materialia 59 (2011) 2035–2045.

[22] X. Guo, R. Waser, Electrical properties of the grain boundaries of oxygen ion conductors: acceptor-doped zirconia and ceria, Progress in Materials Science 51 (2006) 151–210.

[23] X. Guo, W. Sigle, J. Maier, Blocking grain boundaries in yttria-doped and undoped ceria ceramics of high purity, Journal of the American Ceramic Society 86 (2003) 77–87.